
White Rose Research Online

eprints@whiterose.ac.uk
https://eprints.whiterose.ac.uk
Universities of Leeds, Sheffield and York

Deposited via The University of Leeds.

White Rose Research Online URL for this paper:
https://eprints.whiterose.ac.uk/id/eprint/246901/

Version: Accepted Version

Article:
Zhang, H., Chen, Y., Wignall, P.B. et al. (2026) Orbital forcing of paleoclimate and sedimentation in the Early Triassic: Insights from the Dayulin Section, North China. Science China Earth Sciences, 69. pp. 3306-3320. ISSN: 1674-7313

https://doi.org/10.1007/s11430-026-1953-3

Reuse
This article is distributed under the terms of the Creative Commons Attribution (CC BY) licence. This licence allows you to distribute, remix, tweak, and build upon the work, even commercially, as long as you credit the authors for the original work. More information and the full terms of the licence here: https://creativecommons.org/licenses/

Takedown
If you consider content in White Rose Research Online to be in breach of UK law, please notify us by emailing eprints@whiterose.ac.uk including the URL of the record and the reason for the withdrawal request.





Orbital forcing of paleoclimate and sedimentation in the Early Triassic: Insights from the Dayulin Section, North China

Haotian ZHANG[1], Yan CHEN[2,3], Paul B. WIGNALL[4], Kaixuan JI[1*], Meng WANG[5], Xiaoyu ZHANG[1], Hanyu ZHU[1], Ren WEI[1], Zhijun JIN[1] & Mingsong LI[1*]

1 Key Laboratory of Orogenic Belts and Crustal Evolution, School of Earth and Space Sciences, Peking University, Beijing 100871, China

2 State Key Laboratory of Biogeology and Environmental Geology, School of Earth Sciences, China University of Geosciences, Wuhan 430074, China

3 College of Urban and Environmental Sciences, Hubei Normal University, Huangshi 435002, China

4 School of Earth and Environment, University of Leeds, Leeds LS2 9JT, UK

5 State Key Laboratory of Palaeobiology and Stratigraphy, Nanjing Institute of Geology and Palaeontology, Chinese Academy of Sciences, Nanjing 210008, China

* Corresponding authors: Kaixuan JI (jikaixuan_cug@163.com), Mingsong LI (msli@pku.edu.cn)

Abstract

The Early Triassic witnessed dramatic climatic and environmental perturbations following the Permian-Triassic mass extinction. However, terrestrial responses to orbitally forced climate change remain poorly constrained, largely due to the limited availability of high-resolution chronological frameworks. Here, we apply time series analysis of natural gamma-ray logs and the first principal component of X-ray fluorescence elemental data from a terrestrial succession at the Dayulin section in North China (Sunjiagou-Liujiagou-Heshanggou formations). This study establishes a floating astronomical time scale by tuning the paleoclimate proxy series to the 405 kyr long-eccentricity cycle. Integrated with cycle-calibrated magnetostratigraphy, it provides a robust chronological framework for stratigraphic interpretation and inter-section correlation. Applying the sedimentary noise model to the tuned paleoclimate proxy series, we identify intervals of enhanced sedimentary noise that align with major facies transitions, suggesting that climatic instability may have influenced changes in the depositional regime. This study further reveals a 1.2 Myr obliquity modulation cycle corresponding to the Mars-Earth s4−s3 secular resonance during the Early Triassic, expressed within the sedimentary noise series. The detection of this modulation in a low-latitude continental succession highlights the influence of long-term orbital forcing on terrestrial hydroclimate and depositional stability. Moreover, our results provide a new reference framework for Early Triassic terrestrial astrochronology and a geological constraint for refining future astronomical solutions and inter-basin correlations.

Keywords Cyclostratigraphy, Astronomical time scale, Magnetostratigraphic correlation, Sedimentary noise, Early Triassic

1. Introduction

The Permian-Triassic mass extinction was followed by a cascade of environmental crises, including global warming, ocean anoxia, ocean acidification, and recovery of marine and terrestrial ecosystems (Chen and Benton, 2012; Clarkson et al., 2015; Dai et al., 2023; Grasby et al., 2012; Song et al., 2013; Sun et al., 2012). Early Triassic climatic and hydrological fluctuations resulted in regionally variable sedimentary responses, reflecting complex interactions between climatic forcing and depositional systems. Although these responses have been extensively studied in marine sections (Jurikova et al., 2020; Li et al., 2018a; Song et al., 2015; Wei

et al., 2015), high-resolution terrestrial records are geographically limited— primarily to the Germanic Basin (Kozur and Bachmann, 2008; Lucas, 2010; Szurlies et al., 2012), thereby hindering marine-terrestrial correlations. Moreover, in some extinction scenarios, terrestrial environmental perturbations have been shown to trigger knock-on effects in the ocean (Benton and Newell, 2014; Sun et al., 2018). Recent evidence from the North China Basin suggests that terrestrial ecosystem collapse may have preceded the marine mass extinction (Guo et al., 2022), emphasizing the asynchrony between marine and terrestrial crises. Therefore, studying terrestrial sedimentation during hothouse intervals is essential for understanding continental responses to climate change and improving marine-terrestrial correlations.

Identifying past climate changes in terrestrial settings and correlating them with marine records remains challenging, primarily because robust chronological frameworks and appropriate quantitative approaches are scarce (Wang et al., 2020). Compared to marine deposits, terrestrial strata typically exhibit more complex depositional histories. Recently, numerical models such as the sedimentary noise model have been developed to identify environmental "noise" from paleoclimate proxies (Li et al., 2018a). This approach has proven effective across numerous geological intervals, with results corroborated by independent cyclostratigraphic, magnetostratigraphic, and sedimentary indicators (Liu et al., 2021; Wang et al., 2020; Zhang T et al., 2022; Zhang Z F et al., 2022).

Periodic variations in Earth's orbital parameters—eccentricity, obliquity, and precession—modulate the seasonal and latitudinal distribution of insolation and thereby influence the climate system (Hays et al., 1976; Hinnov, 2013). These cyclical forcings are preserved in sedimentary sequences as rhythmic variations in paleoclimate proxies, providing the basis for astronomical tuning. Cyclostratigraphy utilizes paleoclimate proxies to construct a high-resolution astronomical time scale (ATS), which strengthens stratigraphic chronological control and helps illuminate the mechanisms driving past climate change (Hinnov, 2000). Among astronomical cycles, the 405 kyr eccentricity component (g 2−g 5) is particularly stable throughout the Phanerozoic due to the large mass of Jupiter and is therefore widely used in many ATS studies (Laskar et al., 2004), and is also applicable to highenergy, dynamic sedimentary settings such as fluvial and deltaic environments (Wang et al., 2024).

The Dayulin section in the North China Basin exposes a continuous succession of the Sunjiagou, Liujiagou, and Heshanggou formations, recording a spectrum of depositional facies that reflect astronomically forced climate changes from the Late Permian to the Early Triassic. To assess how orbital forcing shaped these terrestrial environments in the wake of the Permian-Triassic mass extinction, we apply cyclostratigraphic analysis to the Dayulin succession using a sedimentary noise model and integrating sequence stratigraphic interpretations. Our study reveals secular astronomical pacing of sedimentary dynamics throughout the Early Triassic hothouse.

2. Geological background

The North China Block was located at approximately 25°N–30°N on the northeastern margin of the Paleo-Tethys Ocean during the Late Permian to the Early Triassic (Liu et al., 2015; Torsvik and Cocks, 2016) (Fig. 1A). The North China Basin, a large and compositionally diverse terrestrial basin in the central part of the block, was filled with a variety of continental depositional systems, including lacustrine, deltaic, fluvial, alluvial, and aeolian deposits (Ji et al., 2023; Liu et al., 2015; Zhu et al., 2020).

The Dayulin section (34°30′6″N, 112°9′20″E), located in Yiyang County, Henan Province (Fig. 1B), is one of the classic terrestrial Permian-Triassic sections in North China. It provides a continuous and well-exposed stratigraphic succession, consisting of the Sunjiagou, Liujiagou, and Heshanggou formations in ascending order.

The Sunjiagou Formation comprises three intervals (Fig. 2A and 2B). The lower interval consists of grey-green, trough-cross-bedded sandstones interbedded with laminated greenish and grey-black mudstones, representing the Medial Terminal Fan facies association (FA1). The middle interval is dominated by thick (>10 m) purple-red mudstones bearing abundant stratified calcareous paleosol nodules at the base, and is interbedded with thick, tabular- to trough-cross-bedded sandstones (>1.5 m) containing lag conglomerates, characteristic of the Arid Floodplain facies association (FA3). The upper interval comprises rhythmic interbeds of thin purple-red sandstones and mudstones or marls with wave ripples and is assigned to the Coastal Mudplain facies association (FA7) (Ji et al., 2023).

The Liujiagou Formation is dominated by thick, trough cross-bedded purple-red to greyish-purple sandstones, interbedded with laminated purple-red mudstones, muddy siltstones, and siltstones (Fig. 2C). The lower part preserves abundant wave- and current-generated ripples and parallel lamination and sporadically contains storm-generated intraformational conglomerates and microbially induced sedimentary structures (MISS), indicating deposition in shallow-lacustrine to lake-margin settings. In the upper part of the formation, the succession coarsens upward into medium-grained sandstones. These sandstones are dominated by stacked sets of unidirectional cross-stratification and locally contain lag deposits, consistent with braided-river deposition (Ji et al., 2023).

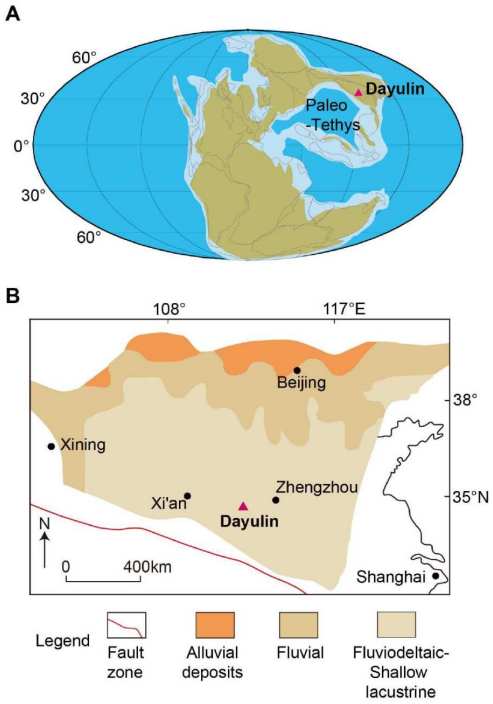


Fig. 1 Paleogeographic maps. (A) Early Triassic global paleogeographic map with the location of the Dayulin section. Modified from http://www.scotese.com; (B) Early Triassic paleogeography of North China. Modified from Zhu et al. (2007).

The Heshanggou Formation is predominantly composed of purple-red siltstones and mudstones, interbedded with thinbedded purple-red sandstones and grey-green sandstones or siltstones (Fig. 2D). The Heshanggou Formation records four facies associations in ascending order: Alluvial Plain with Shallow Lakes (FA6), Coastal Mudplain (FA7), Distal Terminal Fan (FA2), and a return to Alluvial Plain with Shallow Lakes (FA6) (Ji et al., 2023). Our analyses are restricted to the lower part of the Heshanggou Formation, a shallow-lake and coastal plain-dominated interval.

This study focuses on the Sunjiagou Formation (above Bed 3), the Liujiagou Formation, and the lower part of the Heshanggou Formation. The Permian-Triassic boundary (PTB) is inferred to lie within the upper Sunjiagou Formation (Chu et al., 2017, 2019; Guo et al., 2019; Ji et al., 2023; Shu et al., 2022). The Induan-Olenekian boundary (IOB) in the Dayulin section remains uncertain but has been interpreted to lie at the base of magnetic polarity zone DY4n, based on previous magnetostratigraphic studies (Chen, 2020).

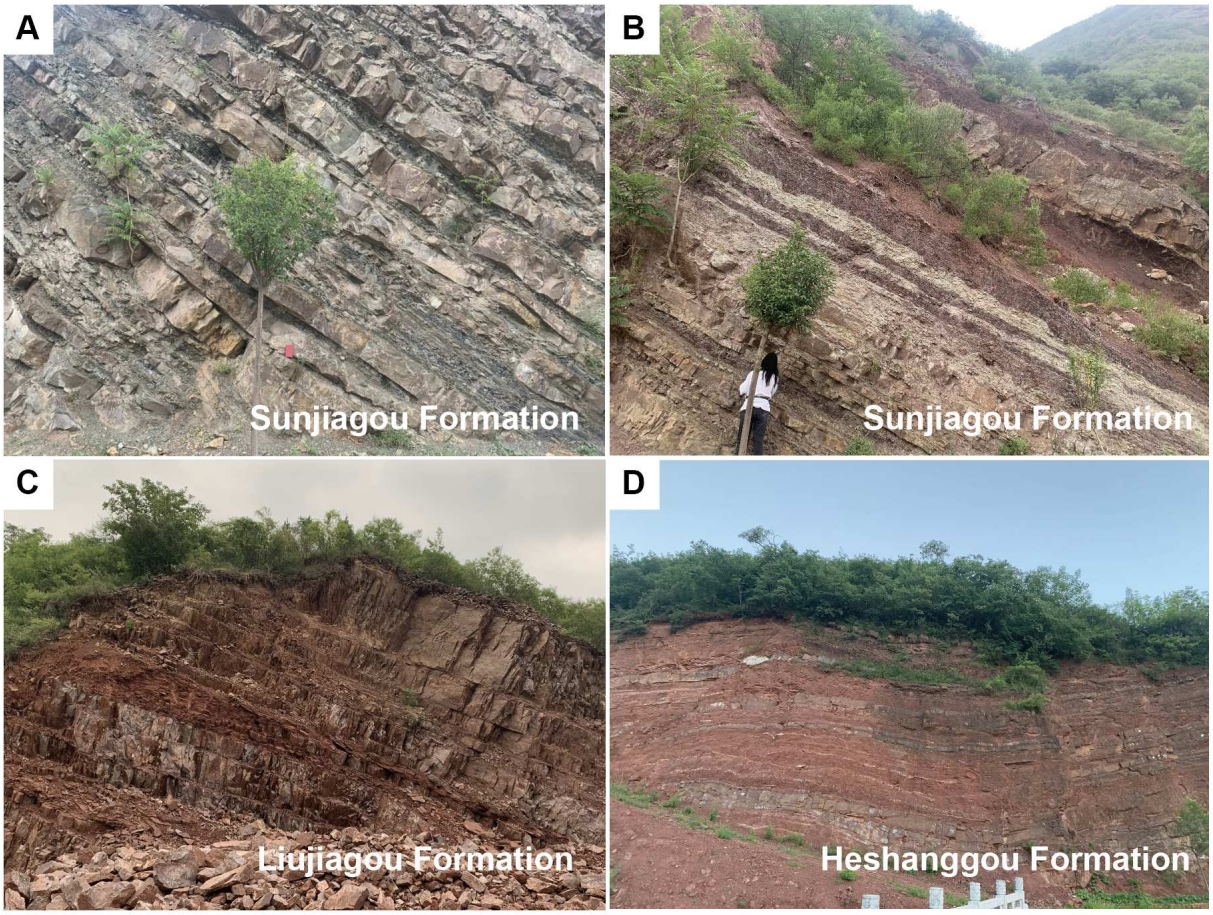


Fig. 2 Outcrops of the Dayulin section. (A) Beds 8–10 of the Sunjiagou Formation (lower part): grey-green to grey-yellow, medium- to thick-bedded fine-grained sandstones interbedded with grey-black to grey-green mudstones, and thin-bedded sandstones; (B) Beds 10–17 of the Sunjiagou Formation (lower to middle part): grey-purple to grey-green siltstone-sandstone alternations; (C) Top of the Liujiagou Formation: grey-purple, thick-bedded, medium- to coarse-grained feldspathic arenites; (D) Base of the Heshanggou Formation: purple-red, thin- to medium-bedded fine sandstones and purple-red mud-siltstone alternations.

3. Materials and methods

3.1 Gamma-ray series

The gamma-ray (GR) intensity of sediments is primarily controlled by the concentrations of uranium (U), thorium (Th), and potassium (K) (Schnyder et al., 2006). U typically accumulates in feldspars, clays, heavy minerals, and organic matter. Th is mainly derived from feldspars, clays, phosphates, and Th-bearing minerals such as monazite. K is commonly concentrated in feldspars, micas, and clays (Schnyder et al., 2006). Climate-driven variations in terrigenous input can be recorded by GR values (Baumgarten and Wonik, 2015), which primarily reflect changes in clay abundance sensitive to continental weathering and runoff, making GR a valuable paleoclimate proxy (Schnyder et al., 2006). Generally, wetter and warmer climates are associated

with enhanced chemical weathering and runoff during high-eccentricity phases, increasing clay and organic matter inputs, thereby leading to higher GR values, whereas cooler and drier periods reduce clay input and lead to lower GR values (van Vugt et al., 2001; Wu et al., 2014). Given its high sensitivity to astronomical forcing and strong signal-to-noise ratio, GR serves as a robust proxy for cyclostratigraphic studies (Li et al., 2019a). In the Dayulin section, GR data were collected using an RS-230 BGO Super-SPEC gamma detector at sampling intervals of 10 cm to 20 cm.

3.2 Elemental concentrations

We used the Thermo Scientific Niton XL5 handheld X-ray fluorescence (XRF) analyzer to measure elemental concentrations in the Dayulin section. A total of 23 elements were analyzed, including Al, Ba, Ca, Cr, Fe, K, Mg, Mn, Nb, Ni, P, Pb, Rb, S, Si, Sn, Sr, Th, Ti, V, Y, Zn, and Zr. To ensure data quality, elements with values below the limits of detection (LOD), as well as those with relative uncertainties greater than 5%, were excluded from further analysis. Based on these criteria, nine elements (Al, Ca, Si, Fe, K, Rb, Sr, Ti, and Zr) were retained for subsequent analysis and selected as paleoenvironmental proxies. Ti, K, Rb, and Zr are commonly used as indicators of detrital input from the catchment (Jin et al., 2006; Kylander et al., 2011). Grain-size variability is often inferred from the Zr/Rb (Kylander et al., 2011) and Al/Si (Clift et al., 2014) ratios. Ca, Sr, and Si may reflect in-lake productivity and hydrological balance (Cohen, 2003; Davison, 1993). Al and Rb are widely considered conservative tracers of terrigenous material (Boës et al., 2011). Fe may be influenced by a wider range of processes, including variations in terrigenous detrital supply, redox conditions, and hydrodynamic sorting related to grain-size changes (Davison, 1993; Kylander et al., 2011; Roy et al., 2013; Schiff and Weisberg, 1999). K/Al, K/Ti, and Rb/K ratios have been used to infer weathering intensity and regime (Brown, 2011; Clift et al., 2014). Lacustrine sedimentary processes are inherently complex, often resulting in highly variable sediment compositions due to interactions among biological, chemical, and physical factors (Boës et al., 2011; Davies et al., 2015). Therefore, a multi-proxy approach is required to robustly interpret sedimentary geochemistry and reconstruct paleoenvironmental changes.

3.3 Principal component analysis

Principal component analysis (PCA) is a multivariate statistical technique that reduces the dimensionality of complex datasets while retaining the main patterns of variance within the original data matrix (Dunteman, 1989). To explore the primary geochemical characteristics, PCA was performed in MATLAB using the selected XRF-derived elemental variables. The first three principal components explain 36.1%, 21.7%, and 11.3% of the total variance (Appendix Fig. S1), respectively, with the first principal component (PC1) accounting for the largest proportion of the variance. The element loadings indicate that PC1 is primarily controlled by K, Rb, Al, and Fe, with secondary contributions from Ti and Zr, whereas Ca exhibits a moderate negative loading and Si and Sr contribute only weakly (see the Supplementary Material for more details). Because orbital-scale insolation forcing can influence atmospheric circulation and climatic belts (Matthews and Perlmutter, 1994), thereby modulating weathering, runoff, erosion, and sedimentation processes (Strasser et al., 2006), such changes can be recorded by climate-sensitive geochemical proxies. Therefore, the high loadings of K, Rb, Al, Fe, Ti, and Zr, together with the contribution of Ca, suggest that PC1 may reflect variations in sediment source and associated changes in sediment composition. In this study, PC1 likely captures the dominant paleoenvironmental signal in the XRF dataset and may also record paleoclimatic variability.

3.4 Time series analysis

Time series analysis was conducted to identify astronomical signals and construct an ATS for the Dayulin section.

(1) Detrending. To remove long-term non-Milankovitch trends, the data were detrended using Locally Estimated Scatterplot Smoothing (LOESS) (Cleveland and Devlin, 1988).

(2) Spectral analysis. The Multi-Taper Method (MTM) (Thomson, 1982) was employed for spectral analysis, and Smoothed Window Averaging (SWA) (Weedon et al., 2019) was applied to estimate background spectral noise and assist in identifying depositional cyclicity. The statistical significance of MTM spectral peaks was assessed using the SWA and the false discovery rate (FDR) approach (Weedon et al., 2019) in combination with robust red noise modeling (Jiang et al., 2025).

(3) Sedimentation rate estimation. Statistical tuning approaches, including correlation coefficient (COCO), evolutionary COCO (eCOCO), and Average Spectral Misfit (ASM), were used to estimate the average sedimentation rate (Li et al., 2018b; Meyers and Sageman, 2007). COCO evaluates a series of test sedimentation rates by converting paleoclimate proxy data into time series, computing the correlation between their power spectra and astronomical solutions. High correlation coefficients and a low null-hypothesis level were used to identify the optimal sedimentation rates. The eCOCO method was further applied to track variations in sedimentation rate with depth using a sliding window approach (Li et al., 2018b). ASM evaluates the difference between observed spectral peak frequencies and target astronomical frequencies for estimating sedimentation rates and testing the null hypothesis of no orbital forcing (Meyers and Sageman, 2007).

(4) Cycle identification and filtering. Based on the estimated sedimentation rates, cycle ratios, and the astronomical solution of Laskar et al. (2004), specific periodicities were interpreted as representing orbital cycles. Recent stochastic sedimentation models indicate that terrestrial records tend to lose higher-frequency cycles due to disturbance, whereas lower-frequency signals, such as the 405 kyr eccentricity cycle, are more likely to be preserved (Wang et al., 2024). Given the diverse depositional environments and relatively continuous stratigraphy of the Dayulin section, we selected the 405 kyr long-eccentricity cycle for astronomical tuning. The 405 kyr long-eccentricity component was extracted using Gauss bandpass filtering (Kodama and Hinnov, 2014) and subsequently employed for astronomical age model construction. Focusing on this low-frequency signal enhances the robustness of cyclostratigraphic correlations by reducing susceptibility to distortion or erosion.

(5) Tuning. The depth series were tuned to the time domain using the constructed age model to create a floating ATS.

All analyses were performed using Acycle v2.8 software (Li et al., 2019b; Li, 2026) and the astrochron v1.2 R package (Meyers, 2014).

3.5 Sedimentary noise model

The sedimentary noise model integrates two approaches: The dynamic noise after orbital tuning (DYNOT) method and lag-1 autocorrelation coefficient (ρ1) analysis. The DYNOT method quantifies noise in proxy by assessing the variance ratio between orbitally forced signals and non-orbital components (Li et al., 2018a). The ρ1 method utilizes the lag-1 (first-order) autocorrelation coefficient as an independent indicator of noise level (Li et al., 2018a). In general, higher DYNOT values (reflecting greater noise) are coupled with lower ρ1, and vice versa. The sedimentary noise model has proven effective in reconstructing noise level fluctuations in both marginal marine and lacustrine settings (Li et al., 2018a; Wang et al., 2020; Zhang T et al., 2022).

4. Results

4.1 Time series analysis

To address changes in sedimentation rate and avoid bias in sedimentation rate estimation caused by pronounced variability (Meyers and Sageman, 2007), GR and XRF PC1 data from the Dayulin section were divided into three depth intervals: Segment 1 (0–75 m), Segment 2 (75–185 m), and Segment 3 (≥185 m) (Figs.

3–5), based on the eCOCO analysis (Fig. 5), which shows that there are obvious shifts in the optimal sedimentation rate at ~75 m and ~185 m.

In Segment 1 (0–75 m, from the basal part of the section to the upper Sunjiagou Formation), GR shows a significant spectral peak at approximately 18 m that exceeds the 5% FDR threshold, and a corresponding peak is observed in XRF PC1. Accordingly, the ~18 m wavelength is regarded as a reliably preserved regular wavelength (Weedon et al., 2019). The spectral peaks at 2.8, 1.5, and ~1.1 m in GR (Fig. 4A) and at 4.8, 3.9, 1.6, 1.4, and 1.1 m in XRF PC1 (Fig. 4B), all exceed the 95% χ2 confidence level. The ratios of the significant wavelengths (~18 m:~4.8 m:~1.5 m: ~1.1 m) generally match the periodicity ratios of La2004 astronomical solution (Laskar et al., 2004) at 244–249 Ma (405 kyr:~100 kyr:~33 kyr:~20 kyr).

In Segment 2 (75–185 m, uppermost Sunjiagou to middle Liujiagou Formation), the GR spectrum reveals prominent peaks at 36, 6.2, ~2.4, ~1.6, ~1.1, and 1.0 m (Fig. 4C), and XRF PC1 shows similar peaks at 36, 3.4, 2.6, ~1.6, 1.4, and 1.1 m (Fig. 4D). All peaks exceed the 95% χ2 confidence level. The ratios of the significant wavelengths (~36 m:~3.4 m:~1.6 m) generally match the periodicity ratios of La2004 astronomical solution (Laskar et al., 2004) at 244–249 Ma (405 kyr:~33 kyr:~20 kyr).

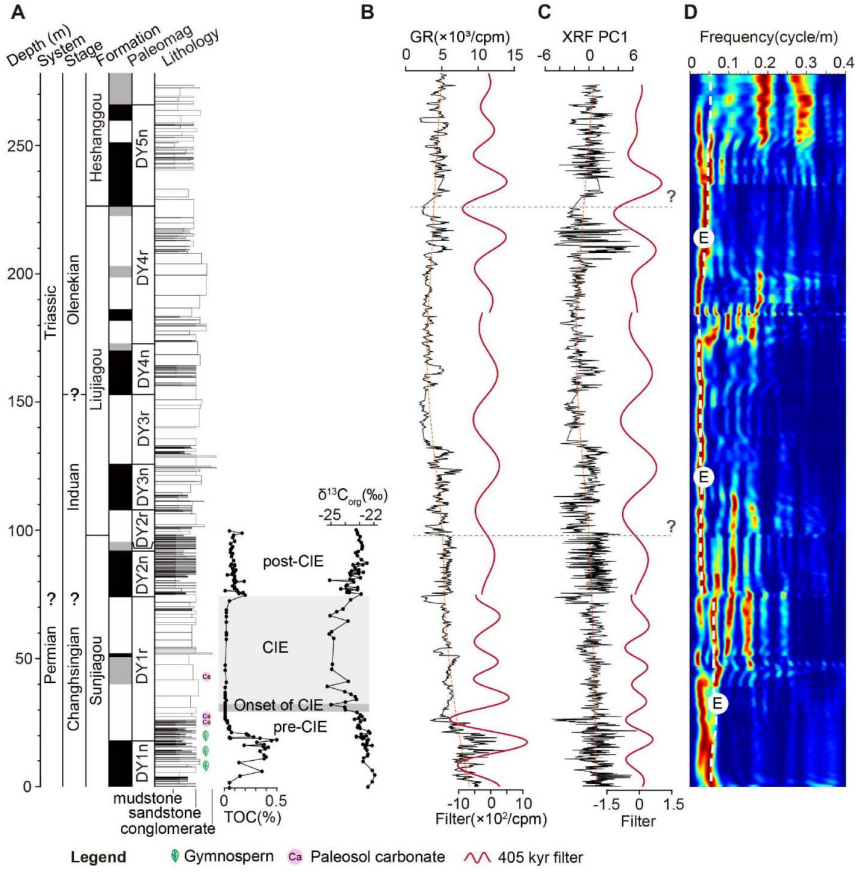


Fig. 3 Integrated stratigraphy of the Dayulin section. (A) Magnetic polarity zones (Chen, 2020), lithology, TOC and $\delta^{13}C_{org}$ (Wu et al., 2020); (B) GR series with a 60% weighted LOESS trend (orange dashed line), and filtered 405 kyr cycle-related wavelengths (red solid line; Gauss filter, passband: 0.055±0.025 cycles/m for the 0–75 m interval, 0.0275±0.0075 cycles/m for the 75–185 m interval, and 0.045±0.015 cycles/m for the 185–278 m interval); (C) XRF PC1 series with a 60% weighted LOESS trend (orange dashed line), and filtered 405 kyr cycle-related wavelengths (red solid; Gauss filter, passband: 0.055±0.025 cycles/m for the 0–75 m interval, 0.0275±0.0075 cycles/m for the 75–185 m interval, and 0.04±0.02 cycles/m for the 185–274 m interval). The grey dashed lines indicate possible gaps near stratigraphic boundaries; (D) Evolutionary power spectrum of the

GR data (colored plot), calculated using a 50 m running window. The 405 kyr eccentricity cycles are marked with white circles and white dashed lines.

In Segment 3 (≥185 m, upper Liujiagou to the lower Heshanggou Formation), GR is characterized by spectral peaks at 22, 5.4, ~3.4, ~2, 1.4, and 1.2 m (Fig. 4E), while XRF PC1 displays notable peaks at 23, 3.4, ~2.2, 1.4, and 1.1 m (Fig. 4F); all peaks exceed the 95% $\chi 2$ confidence level. The ratios of the significant wavelengths (~22 m:~5.4 m:~2 m:~1.1 m) largely match the periodicity ratios of La2004 astronomical solution (Laskar et al., 2004) at 244–249 Ma (405 kyr:~100 kyr:~33 kyr:~20 kyr). Other periodicities in the Dayulin section may reflect changes in sedimentation rate, regional climate variability, and/or bioturbation in the terrestrial depositional setting.

The COCO analyses of the GR and XRF PC1 series reveal three prominent sedimentation rate peaks at approximately 1.5–1.6, 5, and 9 cm/kyr, all of which reject the null hypothesis of no astronomical forcing at the 0.01 significance level (Fig. 5). Segment-based sedimentation rate estimates are as follows: Segment 1: COCO yields ~1.5–1.6 cm/kyr (not supported by cycle ratios) and ~4 cm/kyr; ASM yields ~7.9 cm/kyr (not supported by cycle ratios) (Figs. S2 and S3). Segment 2: COCO and ASM estimates converge on ~9 cm/kyr and ~8 cm/kyr, respectively (Figs. S4 and S5). Segment 3: COCO identifies ~3.5 cm/kyr and ~6.5 cm/kyr; ASM produces a comparable estimate of ~6.7 cm/kyr (Figs. S6 and S7).

In comparison, the eCOCO results indicate a three-stage variation in sedimentation rate, with relatively low rates (~4–6 cm/kyr) at the base and top of the section, and higher rates (~7–9 cm/kyr) in the middle. This pattern is clearly visible in the eCOCO sedimentation rate map (Fig. 5). Based on cycle ratios and sedimentation rate estimates, we selected the following wavelengths—18 m in Segment 1, 36 m in Segment 2, and 22 m in Segment 3—as representative of the 405 kyr eccentricity cycle for constructing the age model. The linear sedimentation rate model derived from long-eccentricity tuning is consistent with the eCOCO results (Fig. 5). After astronomical tuning, spectral analysis of the tuned GR and XRF PC1 series reveals prominent astronomical cycles (Fig. 6B and 6C), which closely align with the predicted periodicities of the La2004 astronomical solution (Laskar et al., 2004) (Fig. 6D).

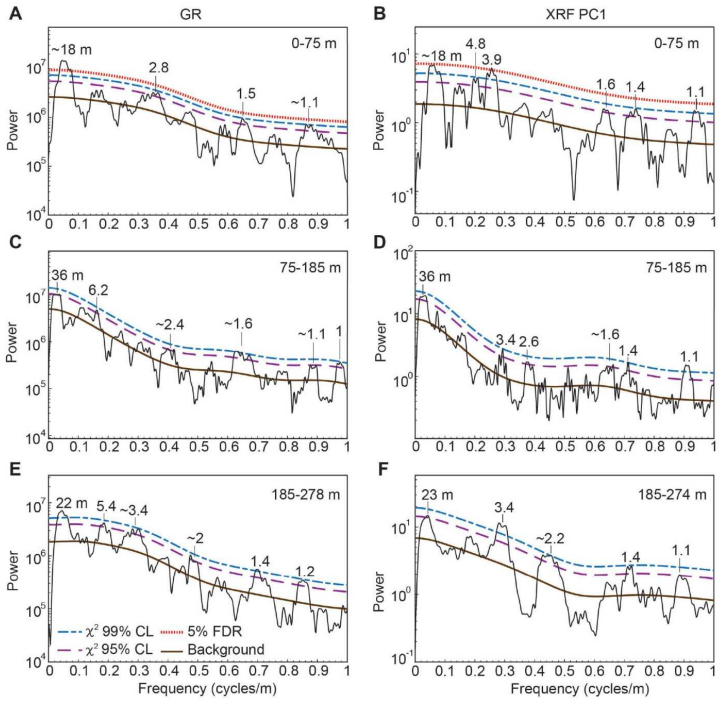


Fig. 4 2π MTM power spectral analysis of GR (A, C, E) and XRF PC1 (B, D, F) series. Significance levels are assessed using the smoothed window average (SWA) background and the false discovery rate (FDR) method. CL–confidence level; FDR–false discovery rate. Only peaks exceeding the 95% χ2 confidence level are labeled.

4.2 Sedimentary noise

We applied the ρ1 and eCOCO methods to evaluate the depositional stability of the Dayulin section using the GR and XRF PC1 series in the depth domain (Fig. 7C, 7E and 7F). Comparison of the results shows that three sedimentation rate shift intervals (70–95 m, 172–200 m, and 227–247 m) coincide with decreases in ρ1 values in both the GR and XRF PC1 records, likely indicating enhanced noise during these periods. We also applied the DYNOT and ρ1 methods to reconstruct the sedimentary noise history using the tuned GR and XRF PC1 series. The DYNOT and ρ1 results (Fig. 7H, 7I, 7K and 7L) exhibit similar patterns, with intervals of enhanced noise in the depth domain corresponding to those in the time domain (grey areas in Fig. 7), indicating that the detected noisy intervals are independent of the timescale.

Spectral analysis of the DYNOT and ρ1 median values from the tuned GR and XRF PC1 series identifies a significant 1.2 Myr cycle that exceeds the 5% FDR threshold (Fig. 8C–8F). Spectral analysis of the amplitude modulation (AM) of eccentricity and obliquity further reveals prominent long-term modulations at 2.5 Myr and 1.2 Myr within the 249–244 Ma interval (Fig. 8A and 8B). However, given that the total duration of the studied interval is approximately 4.8 Myr, longer-period trends over ~2.4 Myr are not considered in this study due to their relatively low confidence.

5. Discussion

5.1 The floating astronomical time scale of the Dayulin section

Previous studies suggest that the PTB in the Dayulin section lies within the upper part of Sunjiagou Formation, above a distinctive, thick, grey-purple Vertisol that can be traced laterally across multiple sections (Chu et al., 2017, 2019; Guo et al., 2019; Ji et al., 2023; Shu et al., 2022; Tu et al., 2016). Magnetostratigraphic results from the Dayulin section reveal a normal polarity zone (DY4n) in the middle part of the Liujiagou Formation, which can be broadly correlated with LT3n in the Geomagnetic Polarity Time Scale (GPTS) (Hounslow and Muttoni, 2010). This interval has been discussed in relation to the IOB (Chen, 2020). Potential hiatuses near formation boundaries could bias estimates of the total depositional duration. Accordingly, the time scale developed in this study is intended to constrain only the preserved stratigraphic record. The durations of any hiatuses are unknown, and their precise quantification remains a major technical challenge beyond the scope of this study. Nevertheless, any such gaps are not expected to compromise the 405 kyr ATS, whereas hiatuses on the ~100 kyr time scale cannot be excluded, particularly across the Sunjiagou-Liujiagou boundary (Ji et al., 2023). Considering the uncertainties in precisely constraining key stratigraphic boundaries within the Dayulin section, we adopt the more stable and well-preserved 405 kyr cycle to establish an ATS, and focus on the astronomical signals recorded in the strata and their implications for paleoclimatic change. The geochronology of the Induan will be discussed in a separate study.

The tuned GR and XRF PC1 series from the Dayulin section show comparable orbital-scale variations, supporting the reliability of the astronomical tuning (Fig. 6). Our cyclostratigraphic analysis indicates that the studied interval preserved approximately 4.8±0.2 Myr (Late Permian to Early Triassic), with the empirical uncertainty corresponding to half of a 405 kyr eccentricity cycle. The floating ATS reveals twelve long eccentricity cycles (405 kyr) from just above bed 3 of the Sunjiagou Formation, through the entire Liujiagou Formation, and into the lower part of the Heshanggou Formation. The GR series was selected as the primary basis for subsequent analyses due to its relatively higher signal-to-noise ratio (Li et al., 2019a) and more stable

expression of orbital-scale cyclicity in this section, whereas the XRF PC1 series was used as a reference for comparison and validation.

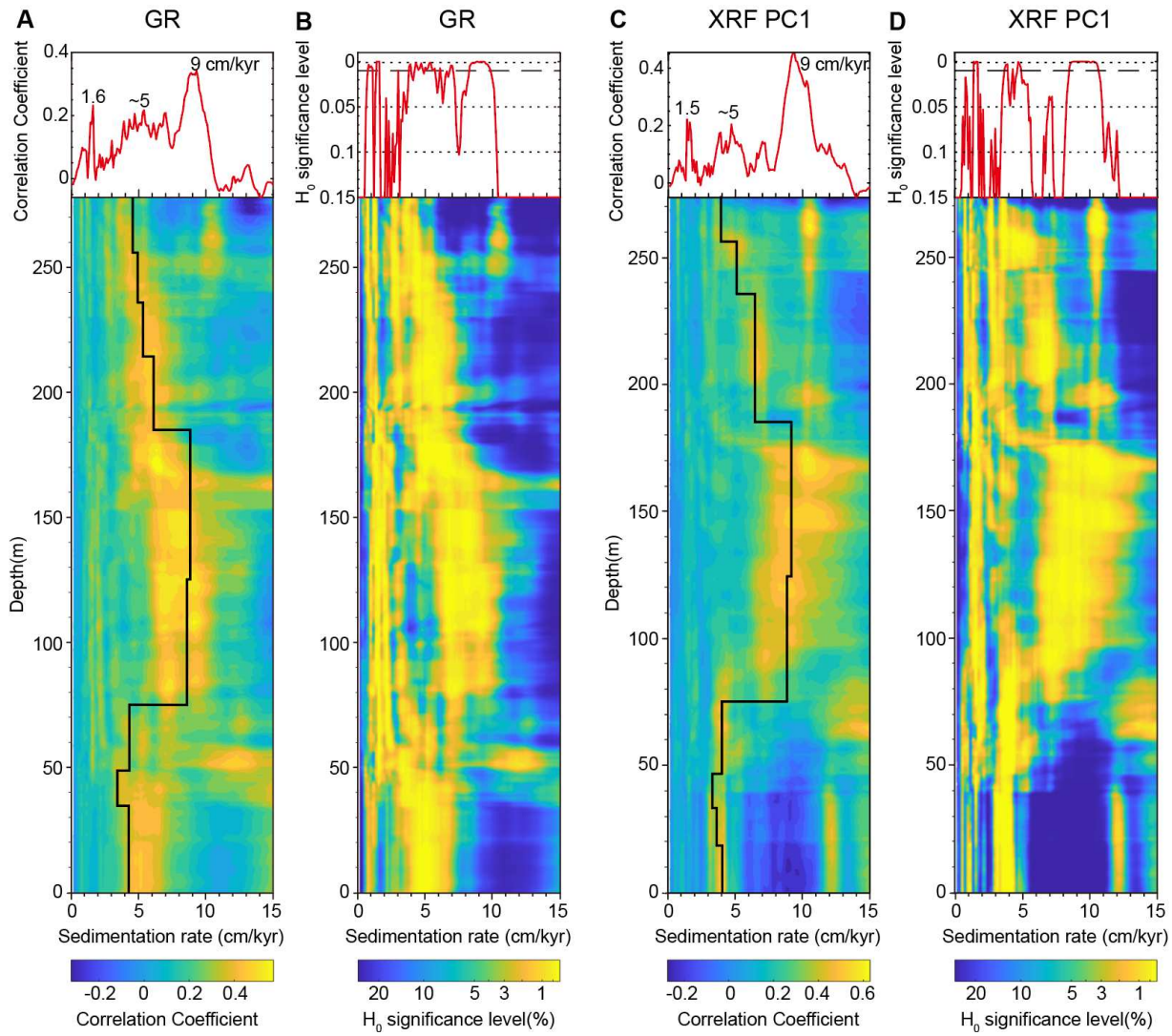


Fig. 5 COCO and eCOCO sedimentation rate analyses of the GR and XRF PC1 series from the Dayulin section. (A and C) Correlation coefficient (top) and evolutionary correlation coefficient (colored area). The black solid lines represent the sedimentation rates derived from long-eccentricity tuning; (B and D) Null hypothesis test (top) and evolutionary null hypothesis (H 0) significance level (colored area). For both COCO and eCOCO analyses, sedimentation rates were tested from 1 to 15 cm/kyr with increments of 0.2 cm/kyr, using 2000 Monte Carlo simulations. For the eCOCO analysis, the sliding window size was set to 60 m, with a step size of 1 m.

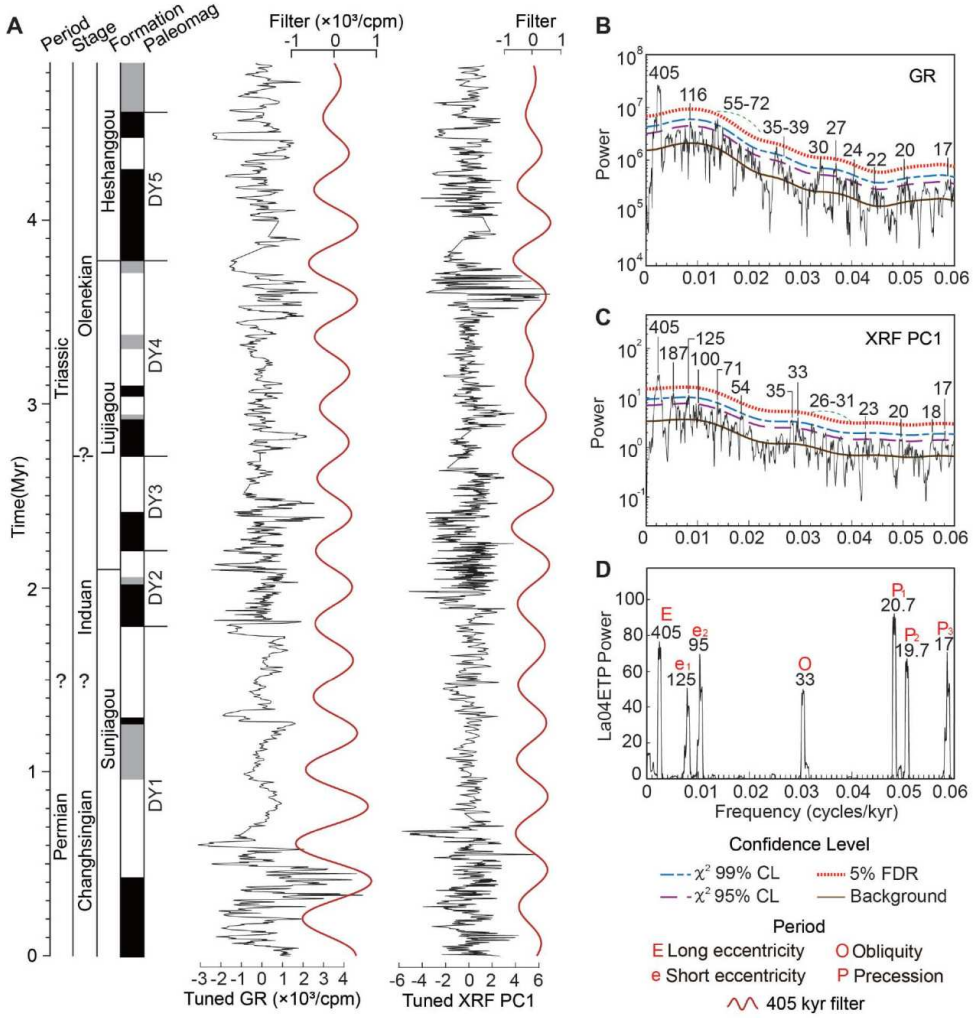


Fig. 6 Tuned cyclostratigraphic results of the GR and XRF PC1 series from the Dayulin section. (A) Integrated stratigraphy of the Dayulin section. Magnetic polarity pattern derived from Chen (2020). Tuned GR series with 405 kyr filters (red curves, passband: 0.00247±0.00049 cycles/kyr). Tuned XRF PC1 series with 405 kyr filters (red curves, passband: 0.00247±0.00049 cycles/kyr). (B) 2π MTM power spectra of the tuned GR series in the time domain. (C) 2π MTM power spectra of the tuned XRF PC1 series in the time domain. Significance levels are assessed using the smoothed window average (SWA) background and the false discovery rate (FDR) method. CL–confidence level; FDR–false discovery rate; E–eccentricity; O–obliquity; P–precession. Only peaks exceeding the 95% χ2 confidence level are labeled. (D) Earth's orbital parameters from the Laskar solution spanning 244–249 Ma, with ETP representing the combined normalized values of eccentricity, tilt, and precession (E:T:P ratios of 1:0.5:1) (Laskar et al., 2004).

5.2 Magnetostratigraphic correlation

We compared the Dayulin section's magnetic polarity zones to multiple references: the Geomagnetic Polarity Time Scale (GPTS, Fig. 9D) (Hounslow and Muttoni, 2010), the GTS2020 magnetic polarity compilation (Fig. 9C) (Ogg et al., 2020), the cycle-calibrated magnetic results from four South China marine sections (Chaohu, Daxiakou, Xiejiacao, and Shangsi; Fig. 9A) (Zhang H T et al., 2025), and the terrestrial Shichuanhe section in North China (Fig. 9E) (Guo et al., 2022). These marine and terrestrial records establish a framework for both regional and global correlation of Dayulin's magnetostratigraphy. According to the GPTS, the Early Triassic comprises several magnetic polarity zones, with the IOB located near the base of the LT3 normal polarity zone (Hounslow and Muttoni, 2010). In these reference sections, this same zone is labeled cLT4n in the integrated

South China section (Zhang H T et al., 2025), SCH5n in the Shichuanhe section (Guo et al., 2022), and DY4n in the Dayulin section (Chen, 2020). Given the relatively distinct polarity pattern near the IOB, that horizon serves as a key tiepoint for inter-section correlation. It is possible that a lowstand systems tract occurs near the Sunjiagou-Liujiagou formation boundary, where a possible discontinuity is indicated in Fig. 3; therefore, non-deposition may have occurred close to the boundary. Under this scenario, the Sunjiagou-Liujiagou boundary could be placed within LT2r. Given the uncertainty associated with possible non-deposition near the Sunjiagou- Liujiagou boundary, magnetostratigraphic correlation in this study is restricted to the stratigraphic interval above DY3.

DY4 spans approximately 1.07 Myr. The base of DY5n corresponds to a trough between two long-eccentricity peaks, and aligns with the base of SCH6n in the Shichuanhe section (Guo et al., 2022) and LT6n in the GPTS (Hounslow and Muttoni, 2010) and GTS2020 (Ogg et al., 2020). This correlation is supported by the combined duration of LT3, LT4, and LT5, which collectively span ~1.2 Myr.

Within the Induan Stage, two major magnetic polarity zones are recognized: LT1 and LT2. The IOB lies above the LT2 polarity zone, while the base of LT2n is situated near the Griesbachian- Dienerian boundary (Hounslow and Muttoni, 2010; Ogg et al., 2020). This polarity boundary correlates with the base of cLT3n in South China, DY3n in the Dayulin section, and SCH4n in the Shichuanhe section. Notably, in the integrated magnetostratigraphy of South China, the base of cLT3n approximately corresponds to the trough between the second and third long-eccentricity cycles. Similarly, the base of DY3n in the Dayulin section aligns with a trough between two eccentricity maxima. The DY3 duration of 0.51 Myr aligns well with cLT3 (0.7 Myr), and LT2 (~0.65 Myr) within error. Given the uncertain position of the PTB, we do not correlate DY1 and DY2 with other sections in this study.

5.3 Sedimentary noise model of environmental instability

Based on the facies model of the Dayulin section, the Sunjiagou Formation, Liujiagou Formation, and the lower part of the Heshanggou Formation record a range of depositional environments: a coastal plain with low-sinuosity fluvial channels in the Sunjiagou Formation; braided fluvial and lacustrine settings in the Liujiagou Formation; and shallow lakes in the Heshanggou Formation (Ji et al., 2023).

This study uses ρ1 and DYNOT to identify sedimentary noise. The ρ1 method measures lag-1 autocorrelation between consecutive time steps and is used as an indicator of the stability of the climate-sedimentation system (Li et al., 2018a). DYNOT independently quantifies variability not attributable to astronomical forcing, highlighting non-orbital noise in the stratigraphic record (Li et al., 2018a). In addition, variations in eCOCO values can also indicate the stability of depositional environments, with stronger eCOCO values indicating more stable environments, and vice versa (Li et al., 2018b; Wang et al., 2020, 2022). Climate fluctuations and tectonically related changes in provenance may modulate sedimentary noise levels (Li et al., 2018a; Meyers and Hinnov, 2010), and such changes may be reflected in the stratigraphic record by enhanced lithological variability and, in some intervals, facies shifts.

This study focuses on interpreting variations in the modeled noise signal as an integrated response to environmental transitions. The intervals of enhanced sedimentary noise in the Dayulin section broadly coincide with major facies transitions (Fig. 7). Thus, the noisy interval from 70 m to 95 m corresponds to a shift from FA3 (arid floodplain) to FA7 (coastal mudplain); the slightly noisy interval from 172 m to 200 m reflects a transition from FA5 (shallow lake-lake margin) to FA4 (low-sinuosity fluvial system); and the noisy interval from 227 m to 247 m marks a transition from FA4 to FA6 (low sinuosity fluvial system to alluvial plain with shallow lakes). The Sunjiagou Formation comprises three facies associations and records a transition from medial terminal fan and arid floodplain settings to coastal mudplain environments (Ji et al., 2023). The lower and middle parts of the formation indicate an overall arid climate (Ji et al., 2023). Depositional shifts in the lower part of the Sunjiagou Formation may provide independent evidence for the environmental instability

indicated by the sedimentary noise signal. The observed correspondence between enhanced sedimentary noise and major facies transitions suggests that noise parameters can serve as indicators of environmental instability in terrestrial depositional settings.

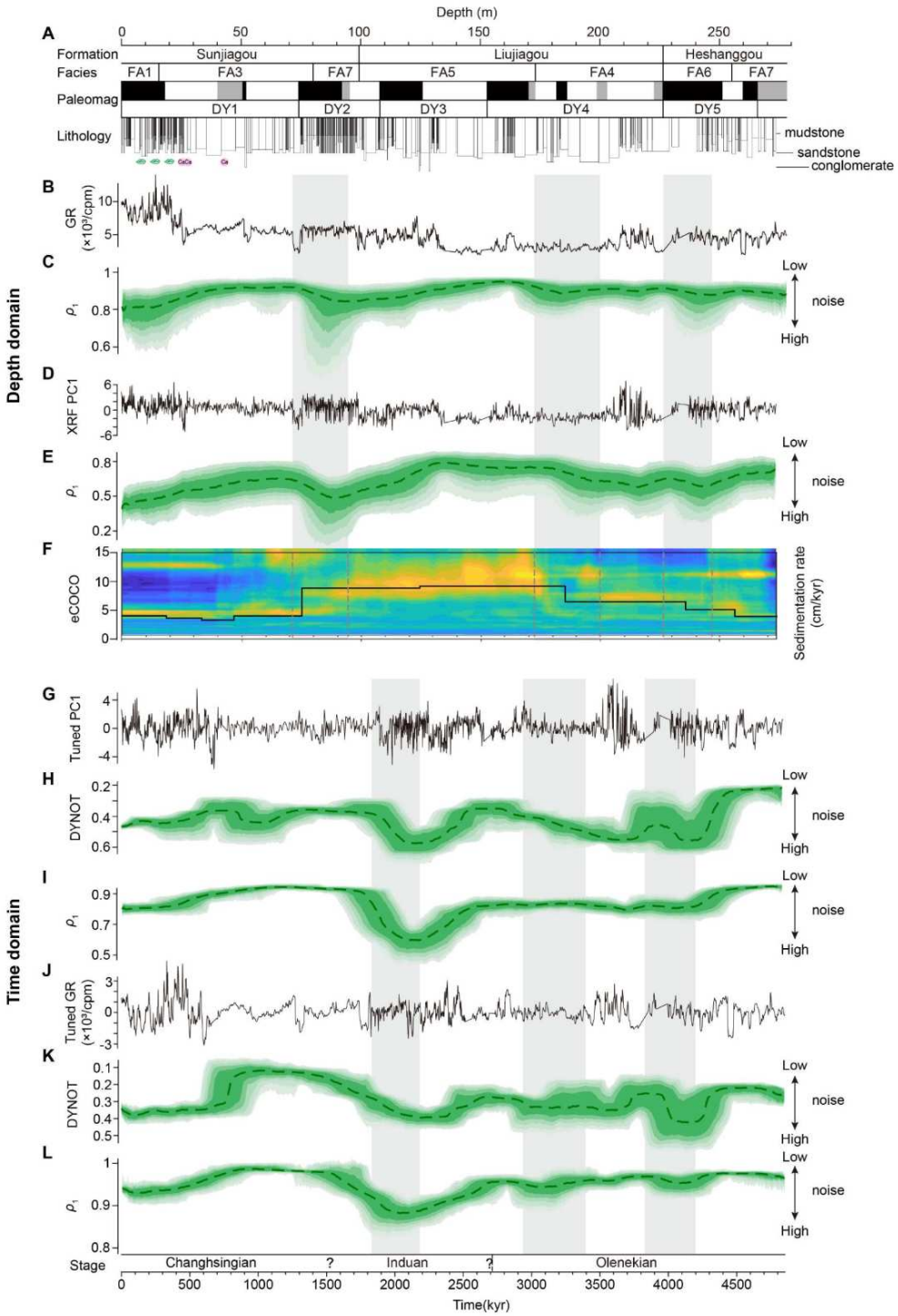


Fig. 7 Sedimentary noise interpretation of the Dayulin section. (A) Magnetic polarity zones (Chen, 2020), facies associations (Ji et al., 2023), and lithology; (B and C) GR series and the corresponding ρ1 results; (D and E) XRF PC1 series and the corresponding ρ1 results; (F) eCOCO results of the XRF PC1 series; (G–I) Astronomically tuned XRF PC1 series and the corresponding DYNOT and ρ1 results; (J–L) Astronomically tuned GR series and the corresponding DYNOT and ρ1 results.

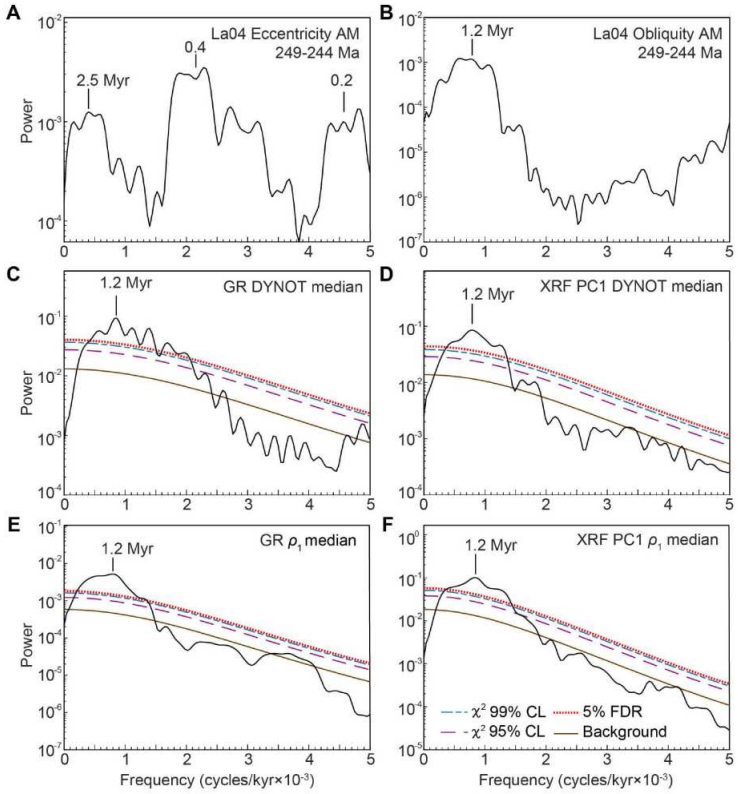


Fig. 8 Results of 2π MTM power spectral analysis. (A and B) Amplitude modulation (AM) of eccentricity (A) and obliquity (B) in the La2004 astronomical solution (Laskar et al., 2004) from 249 Ma to 244 Ma; (C and D) DYNOT median values, with the 3000 kyr LOESS trend removed, based on GR (C) and XRF PC1 (D); (E and F) ρ1 median values, with the 3000 kyr LOESS trend removed, based on GR (E) and XRF PC1 (F). Significance levels are assessed using the smoothed window average (SWA) background and the false discovery rate (FDR) method. CL–confidence level; FDR–false discovery rate.

5.4 Confirmation of the 1.2 Myr Earth-Mars cyclicity

The 1.2 Myr obliquity amplitude modulation (AM) arises from the secular resonance between the s3 and s4 orbital frequencies of Earth and Mars, which govern their inclination evolution (Hinnov, 2000). This "Geological Orrery" has been widely applied to trace ancient Solar System dynamics (Ikeda and Tada, 2020; Laskar et al., 2004; Ma et al., 2017; Olsen et al., 2019). For example, Late Triassic records exhibit 1.6–1.8 Myr eccentricity (g4−g3) and 0.8 Myr obliquity (s4−s3) cycles—distinct from the modern 2.4 Myr cycles in eccentricity and 1.2 Myr cycles in obliquity—yet preserving the characteristic two-to-one ratio of the Earth-Mars resonance, a hallmark of chaotic diffusion in planetary orbits (Sha et al., 2015). However, continuous, multi-Myr, high-resolution sedimentary archives remain scarce, limiting geological confirmation of the canonical 1.2 Myr cycle outside Cenozoic and Late Mesozoic sections.

Only a handful of s4−s3 obliquity modulation records spanning the Triassic have been reported, including ~1.2 Myr from the Early Triassic (Li et al., 2016) and Middle Triassic (Ikeda and Tada, 2020; Liu et al., 2021), ~1.0–~1.3 Myr from the Late Triassic (Wang et al., 2022; Zhang Q et al., 2025; Zhang et al., 2024), and ~0.8 Myr across the Late Triassic to Early Jurassic interval (Sha et al., 2015). These variable periodicities highlight the inherent instability of the Earth-Mars resonance through deep time.

In the Dayulin section, sedimentary noise variations exhibit a significant 1.2 Myr cycle (Fig. 8C–8F). Spectral comparison of eccentricity and obliquity AM between 249 and 244 Ma (Fig. 8A and 8B) confirms that this

dominant signal corresponds to the s4 −s3 obliquity modulation. Consequently, our data demonstrate that the Early Triassic maintained the same 1.2 Myr obliquity periodicity as the Cenozoic, providing geologic evidence for long- term inclination interactions between Earth and Mars and offering new constraints on ancient Solar System dynamics.

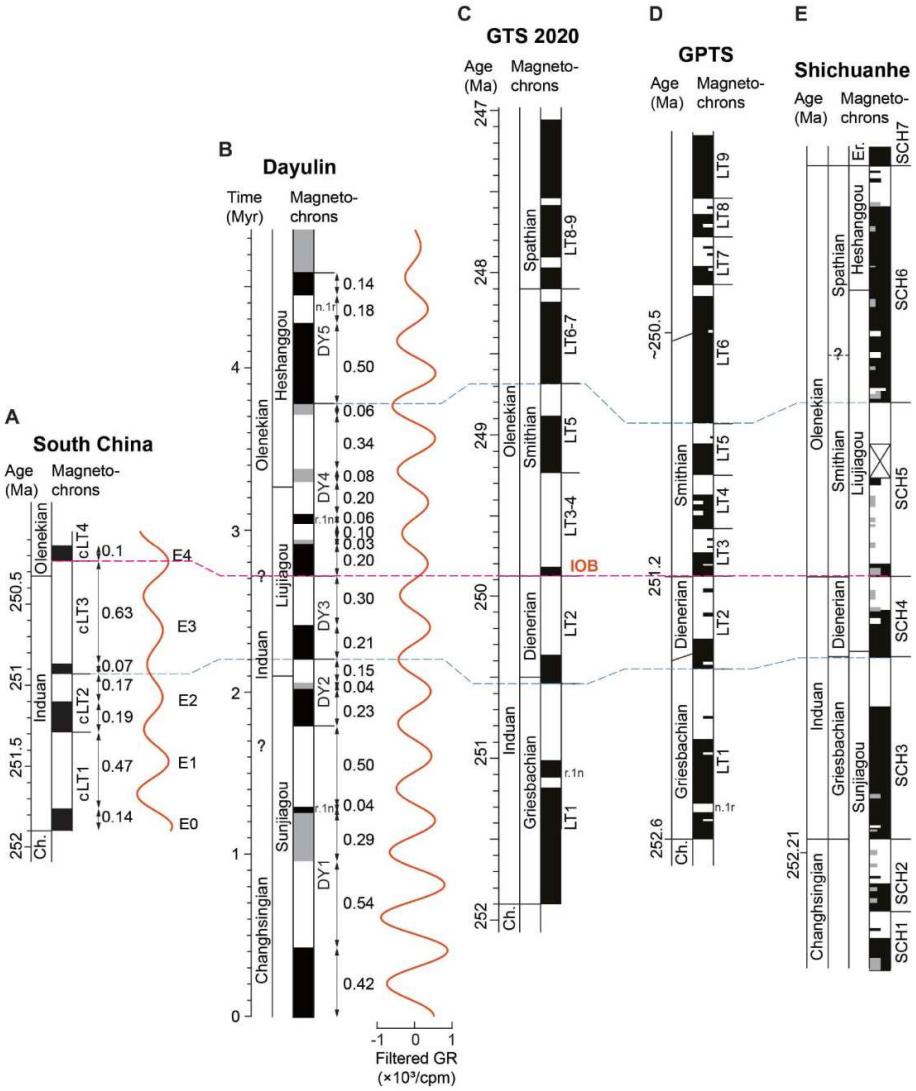


Fig. 9 Magnetic polarity patterns of marine and terrestrial sections in the Early Triassic. (A) 405 kyr cycle calibrated magneto-stratigraphy based on the Chaohu, Daxiakou, Xiejiacao, and Shangsi sections in South China (Zhang H T et al., 2025); (B) 405 kyr cycle calibrated magnetostratigraphy of the Dayulin section (this study); (C) Magnetic polarity pattern from GTS2020 (Ogg et al., 2020); (D) Composite magnetic polarity pattern from Geomagnetic Polarity Time Scale (Hounslow and Muttoni, 2010); (E) Magnetic polarity pattern of the Shichuanhe section (Guo et al., 2022). Dashed lines indicate proposed correlations between polarity zones.

5.5 Myr-scale paleoclimate oscillations

The 1.2 Myr Earth-Mars obliquity AM cycle is now recognized as a fundamental long-term driver of Earth's climate. In the Cenozoic, AM minima coincide with glacial maxima and third-order glacio-eustatic lowstands—when reduced high-latitude insolation facilitates ice-sheet growth—whereas AM maxima mark interglacial highstands (Lourens and Hilgen, 1997; Pälike et al., 2006). Under hothouse conditions, 1.2 Myr

Earth-Mars cycle maxima have been linked to an invigorated hydrological cycle, with enhanced heat and moisture transport driving intensified precipitation (Li et al., 2016; Wendler et al., 2014, 2016). Across multiple time intervals, these obliquity AM extrema align with documented fluctuations in hydrological changes (Li et al., 2016, 2018a; Liu et al., 2021; Wang et al., 2020; Zhang T et al., 2022), reflecting periodic modulation of water exchange between oceanic and continental reservoirs, and corresponding changes in groundwater storage and discharge (Li et al., 2018a, 2023).

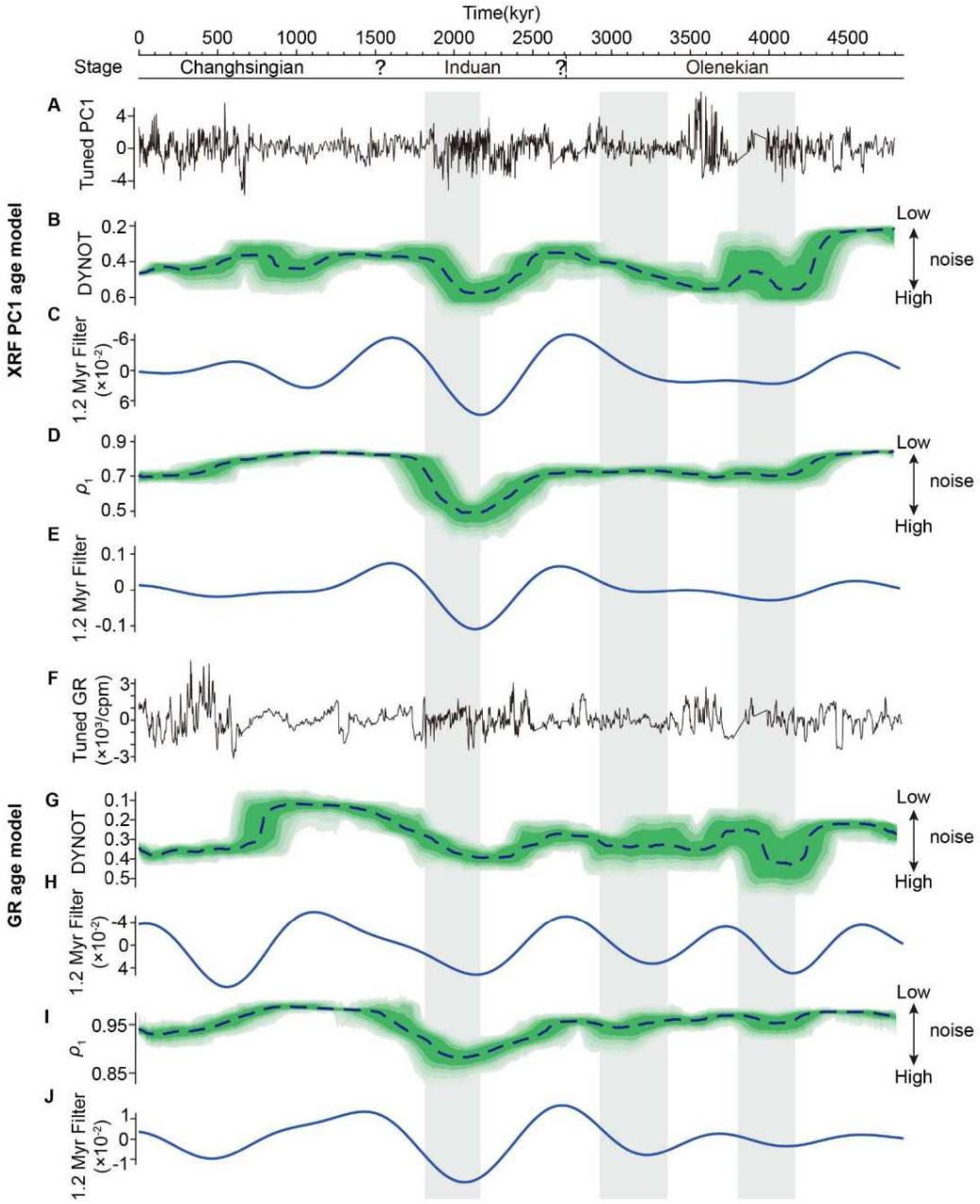


Fig. 10 Correlation of sedimentary noise changes with the 1.2 Myr obliquity amplitude modulation pattern in the Dayulin section. (A) Astronomically tuned XRF PC1 series; (B and C) DYNOT results of the tuned XRF PC1 and the corresponding 1.2 Myr obliquity modulation; (D and E) ρ1 results of the tuned XRF PC1 and the 1.2 Myr obliquity modulation; (F) Astronomically tuned GR series; (G and H) DYNOT results of the tuned GR and the corresponding 1.2 Myr obliquity modulation; (I and J) ρ1 values of the tuned GR and the 1.2 Myr obliquity modulation.

In the Dayulin section, the node of the 1.2 Myr obliquity AM cycle—when obliquity variability is minimal—coincides with intervals of elevated sedimentary noise and facies shifts (Fig. 10). Early Triassic strata at Chaohu and Daxiakou sections of South China similarly record the 1.2 Myr obliquity signal alongside pronounced climatic perturbations, biotic upheavals, and sea-level oscillations (Li et al., 2016). This suggests that the 1.2 Myr obliquity AM cycle may modulate Early Triassic climate-hydrological variability and depositional stability at the regional scale.

Our new findings indicate three implications. First, although obliquity forcing is classically viewed as a high-latitude phenomenon, its clear expression in low-latitude sections (Dayulin, Chaohu, and Daxiakou) underscores a hemispheric-scale influence during the Early Triassic hothouse. Second, the ~1.2 Myr obliquity AM appears to be a persistent regulator of climate, hydroclimate variability, and depositional processes in both terrestrial and marine settings. Third, the obliquity AM pattern provides a powerful correlation tool between continental and marine records, helping to anchor global climate events in deep time.

6. Conclusions

By analyzing gamma-ray data and the first principal component of X-ray fluorescence elemental data from the Dayulin section in North China, we construct a floating astronomical time scale for the Early Triassic, encompassing the Sunjiagou, Liujiagou, and lower Heshanggou formations. The cycle-calibrated magnetostratigraphy at Dayulin shows strong comparability with other sections, enabling high-resolution correlation with both terrestrial and marine records. By applying statistical tuning approaches together with the sedimentary noise model, we identify intervals of elevated sedimentary instability that coincide with facies transitions. We also detect the 1.2 Myr obliquity modulation cycle in the sedimentary noise series from the Dayulin section. Its expression in the low-latitude terrestrial succession demonstrates the influence of long-term orbital forcing on climate and hydrology and indicates that such signals can be preserved in complex continental stratigraphic records. This represents the robust identification of the 1.2 Myr s4−s3 obliquity modulation in Early Triassic terrestrial strata and provides a critical geological constraint for improving the precision and accuracy of future astronomical solutions.

Acknowledgement We thank Prof. James G. OGG and Zhixin WANG for constructive suggestions, and Haoxun ZHANG for his assistance with the fieldwork. Prof. Daoliang CHU is acknowledged for the guidance at the outcrop. This work was supported by the National Natural Science Foundation of China (Grant Nos. 42302031, 42472050 & 42402030). This work was supported by the High- Performance Computing Platform of Peking University. This paper is a contribution to the “Deeptime Digital Earth” Big Science Program.

References

Baumgarten H, Wonik T. 2015. Cyclostratigraphic studies of sediments from Lake Van (Türkiye) based on their uranium contents obtained from downhole logging and paleoclimatic implications. Int J Earth Sci-Geol Rund, 104: 1639–1654

Benton M J, Newell A J. 2014. Impacts of global warming on Permo-Triassic terrestrial ecosystems. Gondwana Res, 25: 1308–1337

Boës X, Rydberg J, Martinez-Cortizas A, et al. 2011. Evaluation of conservative lithogenic elements (Ti, Zr, Al, and Rb) to study anthropogenic element enrichments in lake sediments. J Paleolimnol, 46: 75–87

Brown E T. 2011. Lake Malawi’s response to “megadrought” terminations: Sedimentary records of flooding, weathering and erosion. Palaeogeogr Palaeoclimatol Palaeoecol, 303: 120–125

Chen Y. 2020. Magnetostratigraphy timescale in South China during the Paleozoic-Mesozoic upheavals and its global correlation (in Chinese). Dissertation for Doctoral Degree. Wuhan: China University of Geosciences(Wuhan)

Chen Z Q, Benton M J. 2012. The timing and pattern of biotic recovery following the End-Permian mass extinction. Nat Geosci, 5: 375–383

Chu D, Tong J, Bottjer D J, et al. 2017. Microbial mats in the terrestrial Lower Triassic of North China and implications for the Permian-Triassic mass extinction. Palaeogeogr Palaeoclimatol Palaeoecol, 474: 214–231
Chu D, Tong J, Benton M J, et al. 2019. Mixed continental-marine biotas following the Permian–Triassic mass extinction in South and North China. Palaeogeogr Palaeoclimatol Palaeoecol, 519: 95–107
Clarkson M O, Kasemann S A, Wood R A, et al. 2015. Ocean acidification and the Permo-Triassic mass extinction. Science, 348: 229–232
Cleveland W S, Devlin S J. 1988. Locally weighted regression: An approach to regression analysis by local fitting. J Am Statistical Assoc, 83: 596–610
Clift P D, Wan S, Blusztajn J. 2014. Reconstructing chemical weathering, physical erosion and monsoon intensity since 25 Ma in the Northern South China Sea: A review of competing proxies. Earth-Sci Rev, 130: 86– 102
Cohen A S. 2003. Paleolimnology: The History and Evolution of Lake Systems. Oxford: Oxford University Press
Dai X, Davies J H F L, Yuan Z, et al. 2023. A Mesozoic fossil lagerstätte from 250.8 million years ago shows a modern-type marine ecosystem. Science, 379: 567–572
Davies S J, Lamb H F, Roberts S J. 2015. Micro-XRF core scanning in palaeolimnology: Recent developments. In: Croudace I W, Rothwell R G, eds. Micro-XRF Studies of Sediment Cores: Applications of a Non-De structive Tool for the Environmental Sciences. Dordrecht: Springer. 189– 226
Davison W. 1993. Iron and manganese in lakes. Earth-Sci Rev, 34: 119–163
Dunteman G H. 1989. Principal Components Analysis. Newbury Park: Sage Publications. 96
Grasby S E, Beauchamp B, Embry A, et al. 2012. Recurrent Early Triassic ocean anoxia. Geology, 41: 175–178
Guo W, Tong J, Tian L, et al. 2019. Secular variations of ichnofossils from the terrestrial Late Permian-Middle Triassic succession at the Shichuanhe section in Shaanxi Province, North China. Glob Planet Change, 181: 102978
Guo W, Tong J, He Q, et al. 2022. Late Permian-Middle Triassic magnetostratigraphy in North China and its implications for terrestrial-marine correlations. Earth Planet Sci Lett, 585: 117519
Hays J D, Imbrie J, Shackleton N J. 1976. Variations in the Earth's orbit: Pacemaker of the ice ages. Science, 194: 1121–1132
Hinnov L A. 2000. New perspectives on orbitally forced Stratigraphy. Annu Rev Earth Planet Sci, 28: 419–475
Hinnov L A. 2013. Cyclostratigraphy and its revolutionizing applications in the Earth and planetary sciences. GSA Bull, 125: 1703–1734
Hounslow M W, Muttoni G. 2010. The geomagnetic polarity timescale for the Triassic: Linkage to stage boundary definitions. Geol Soc Lond Spec Publ, 334: 61–102
Ikeda M, Tada R. 2020. Reconstruction of the chaotic behavior of the Solar System from geologic records. Earth Planet Sci Lett, 537: 116168
Ji K, Wignall P B, Tong J, et al. 2023. Sedimentology of the latest Permian to Early Triassic in the terrestrial settings of the North China Basin: Lowlatitude climate change during a warming-driven crisis. GSA Bull, 135: 481–503
Jiang Q, Li M, Yao W, et al. 2025. Astrochronology of the Paleocene–Eocene thermal maximum on the East Tasman Plateau. Glob Planet Change, 252: 104882
Jin Z, Li F, Cao J, et al. 2006. Geochemistry of Daihai Lake sediments, Inner Mongolia, North China: Implications for provenance, sedimentary sort ing, and catchment weathering. Geomorphology, 80: 147–163
Jurikova H, Gutjahr M, Wallmann K, et al. 2020. Permian-Triassic mass extinction pulses driven by major marine carbon cycle perturbations. Nat Geosci, 13: 745–750
Kodama K P, Hinnov L. 2014. Rock Magnetic Cyclostratigraphy. Chichester: Wiley-Blackwell
Kozur H W, Bachmann G H. 2008. Updated correlation of the Germanic Triassic with the Tethyan scale and assigned numeric ages. Ber Geol Bundesanst, 76: 53–58
Kylander M E, Ampel L, Wohlfarth B, et al. 2011. High-resolution X-ray fluorescence core scanning analysis of Les Echets (France) sedimentary sequence: New insights from chemical proxies. J Quat Sci, 26: 109–117

Laskar J, Robutel P, Joutel F, et al. 2004. A long-term numerical solution for the insolation quantities of the Earth. Astron Astrophys, 428: 261– 285
Li M. 2026. Acycle: Enhanced time-series analysis software for geoscience research and education. Sci China Earth Sci, 69: 1066–1071
Li M, Huang C, Hinnov L, et al. 2016. Obliquity-forced climate during the Early Triassic hothouse in China. Geology, 44: 623–626
Li M, Hinnov L A, Huang C, et al. 2018a. Sedimentary noise and sea levels linked to land–ocean water exchange and obliquity forcing. Nat Commun, 9: 1004
Li M, Kump L R, Hinnov L A, et al. 2018b. Tracking variable sedimentation rates and astronomical forcing in Phanerozoic paleoclimate proxy series with evolutionary correlation coefficients and hypothesis testing. Earth Planet Sci Lett, 501: 165–179
Li M, Huang C, Ogg J, et al. 2019a. Paleoclimate proxies for cyclostratigraphy: Comparative analysis using a Lower Triassic marine section in South China. Earth-Sci Rev, 189: 125–146
Li M, Hinnov L, Kump L. 2019b. Acycle: Time-series analysis software for paleoclimate research and education (in Chinese). Comput Geosci, 127: 12–22
Li M, Zhang H, Wang M, et al. 2023. Astronomically forced changes in groundwater reservoirs and sea level during the greenhouse world (in Chinese). Chin Sci Bull, 68: 1517–1527
Liu D, Huang C, Kemp D B, et al. 2021. Paleoclimate and sea level response to orbital forcing in the Middle Triassic of the Eastern Tethys. Glob Planet Change, 199: 103454
Liu Y, Kuang H, Peng N, et al. 2015. Mesozoic basins and associated palaeogeographic evolution in North China. J Palaeogeogr, 4: 189–202
Lourens L J, Hilgen F J. 1997. Long-periodic variations in the Earth's obliquity and their relation to third-order eustatic cycles and Late Neogene Glaciations. Quat Int, 40: 43–52
Lucas S G. 2010. The Triassic Timescale. London: Geological Society of London
Ma C, Meyers S R, Sageman B B. 2017. Theory of chaotic orbital variations confirmed by Cretaceous geological evidence. Nature, 542: 468–470
Matthews M D, Perlmutter M A. 1994. Global cyclostratigraphy: An application to the Eocene Green River Basin. In: de Boer P L, Smith D G, eds. Oxford: Blackwell Scientific Publications. 459–481
Meyers S R. 2014. Astrochron: An R package for astrochronology. http://cran.r-project.org/package=astrochron
Meyers S R, Sageman B B. 2007. Quantification of deep-time orbital forcing by average spectral misfit. Am J Sci, 307: 773–792
Meyers S R, Hinnov L A. 2010. Northern Hemisphere glaciation and the evolution of Plio-Pleistocene climate noise. Paleoceanography, 25: PA3207
Ogg J G, Chen Z-Q, Orchard M J, et al. 2020. The Triassic Period. In: Gradstein F M, Ogg J G, Schmitz M D, et al., eds. Geologic Time Scale 2020. Amsterdam: Elsevier. 903–953
Olsen P E, Laskar J, Kent D V, et al. 2019. Mapping Solar System chaos with the geological orrery. Proc Natl Acad Sci USA, 116: 10664–10673
Pälike H, Norris R D, Herrle J O, et al. 2006. The heartbeat of the Oligocene climate system. Science, 314: 1894–1898
Roy M, McManus J, Goñi M A, et al. 2013. Reactive iron and manganese distributions in seabed sediments near small mountainous rivers off Oregon and California (USA). Cont Shelf Res, 54: 67–79
Schiff K C, Weisberg S B. 1999. Iron as a reference element for determining trace metal enrichment in Southern California coastal shelf sediments. Mar Environ Res, 48: 161–176
Schnyder J, Ruffell A, Deconinck J F, et al. 2006. Conjunctive use of spectral gamma-ray logs and clay mineralogy in defining Late Jurassic-Early Cretaceous palaeoclimate change (Dorset, U.K.) Palaeogeogr Palaeocli matol Palaeoecol, 229: 303–320
Sha J, Olsen P E, Pan Y, et al. 2015. Triassic-Jurassic climate in continental high-latitude Asia was dominated by obliquity-paced variations (Junggar Basin, Ürümqi, China). Proc Natl Acad Sci USA, 112: 3624–3629
Shu W, Tong J, Yu J, et al. 2022. Permian-Middle Triassic floral succession in North China and implications for the great transition of continental ecosystems. GSA Bull, 135: 1747–1767
Song H, Wignall P B, Tong J, et al. 2013. Two pulses of extinction during the Permian-Triassic crisis. Nat Geosci, 6: 52–56
Song H, Wignall P B, Tong J, et al. 2015. Integrated Sr isotope variations and global environmental changes through the Late Permian to early Late Triassic. Earth Planet Sci Lett, 424: 140–147

Strasser A, Hilgen F J, Heckel P H. 2006. Cyclostratigraphy—concepts, definitions, and applications. Newsl Stratigr, 42: 75–114
Sun H, Xiao Y, Gao Y, et al. 2018. Rapid enhancement of chemical weathering recorded by extremely light seawater lithium isotopes at the Permian-Triassic boundary. Proc Natl Acad Sci USA, 115: 3782–3787
Sun Y, Joachimski M M, Wignall P B, et al. 2012. Lethally hot temperatures during the Early Triassic greenhouse. Science, 338: 366–370
Szurlies M, Geluk M C, Krijgsman W, et al. 2012. The continental Permian- Triassic boundary in the Netherlands: Implications for the geomagnetic polarity time scale. Earth Planet Sci Lett, 317-318: 165–176
Thomson D J. 1982. Spectrum estimation and harmonic analysis. Proc IEEE, 70: 1055–1096
Torsvik T H, Cocks L R M. 2016. Earth History and Palaeogeography. Cambridge: Cambridge University Press
Tu C, Chen Z-Q, Retallack G J, et al. 2016. Proliferation of MISS-related microbial mats following the End-Permian mass extinction in terrestrial ecosystems: Evidence from the Lower Triassic of the Yiyang area, Henan Province, North China. Sediment Geol, 333: 50–69
van Vugt N, Langereis C G, Hilgen F J. 2001. Orbital forcing in Pliocene– Pleistocene Mediterranean lacustrine deposits: Dominant expression of eccentricity versus precession. Palaeogeogr Palaeoclimatol Palaeoecol, 172: 193–205
Wang M, Chen H, Huang C, et al. 2020. Astronomical forcing and sedimentary noise modeling of lake-level changes in the Paleogene Dongpu Depression of North China. Earth Planet Sci Lett, 535: 116116
Wang M, Li M, Kemp D B, et al. 2022. Sedimentary noise modeling of lakelevel change in the Late Triassic Newark Basin of North America. Glob Planet Change, 208: 103706
Wang M, Li M, Hajek E A, et al. 2024. Assessing the preservation of orbital signals across different sedimentary environments: Insights from stochastic sedimentation modeling. Earth Planet Sci Lett, 642: 118866
Weedon G P, Page K N, Jenkyns H C. 2019. Cyclostratigraphy, stratigraphic gaps and the duration of the Hettangian Stage (Jurassic): Insights from the Blue Lias Formation of Southern Britain. Geol Mag, 156: 1469–1509
Wei H, Shen J, Schoepfer S D, et al. 2015. Environmental controls on marine ecosystem recovery following mass extinctions, with an example from the Early Triassic. Earth-Sci Rev, 149: 108–135
Wendler J E, Meyers S R, Wendler I, et al. 2014. A million-year-scale astronomical control on Late Cretaceous sea-level. Newsl Stratigr, 47: 1–19
Wendler J E, Wendler I, Vogt C, et al. 2016. Link between cyclic eustatic sealevel change and continental weathering: Evidence for aquifer-eustasy inthe Cretaceous. Palaeogeogr Palaeoclimatol Palaeoecol, 441: 430–437
Wu H, Zhang S, Hinnov L A, et al. 2014. Cyclostratigraphy and orbital tuning of the terrestrial upper Santonian–Lower Danian in Songliao Ba sin, Northeastern China. Earth Planet Sci Lett, 407: 82–95
Wu Y, Tong J, Algeo T J, et al. 2020. Organic carbon isotopes in terrestrial Permian-Triassic boundary sections of North China: Implications for global carbon cycle perturbations. GSA Bull, 132: 1106–1118
Zhang H T, Chen Y, Ogg J G, et al. 2025. Astronomically calibrated integrated stratigraphy of the Induan Stage (Early Triassic) and significance for the Permian-Triassic mass extinction and aftermath. Earth Planet Sci Lett, 669: 119563
Zhang Q, Fu X, Wang J, et al. 2024. Orbitally-paced climate change during the Carnian Pluvial Episode. Earth Planet Sci Lett, 626: 118546
Zhang Q, Fu X G, Su S Q, et al. 2025. Astronomical forcing of the paleoclimate and sedimentary noise modeling of sea-level changes in the Late Triassic. Palaeogeogr Palaeoclimatol Palaeoecol, 659: 112638
Zhang T, Li Y F, Fan T L, et al. 2022. Orbitally-paced climate change in the Early Cambrian and its implications for the history of the Solar System. Earth Planet Sci Lett, 583: 117420
Zhang Z F, Huang Y J, Li M S, et al. 2022. Obliquity-forced aquifer-eustasy during the Late Cretaceous greenhouse world. Earth Planet Sci Lett, 596: 117800
Zhu R, Xu H, Deng S, et al. 2007. Lithofacies palaeogeography of the Permian in Northern China (in Chinese). J Palaeogeogr, 9: 133–142
Zhu Z, Kuang H, Liu Y, et al. 2020. Intensifying aeolian activity following the End-Permian mass extinction: Evidence from the Late Permian-Early Triassic terrestrial sedimentary record of the Ordos Basin, North China. Sedimentology, 67: 2691–2720